Title
Polarization-dependent imaging contrast in abalone shells

Authors
Metzler, Rebecca A.
Zhou, Dong
Abrecht, Mike
et al.

Publication Date
2008-02-15

POLARIZATION-DEPENDENT IMAGING CONTRAST IN ABALONE SHELLS

Rebecca A. Metzler[1], Dong Zhou[1], Mike Abrecht[2], Jinghua Guo[3], Daniel Ariosa[4], Susan N. Coppersmith[1], P.U.P.A. Gilbert[1,*]

[1] *Department of Physics, University of Wisconsin, Madison, WI 53706, USA.*

[2] *Synchrotron Radiation Center, 3731 Schneider Drive, Stoughton, WI 53589, USA.*

[3] *Advanced Light Source, Lawrence Berkeley National Lab, Berkeley CA 94720.*

[4] *Institute for the Physics of Complex Matter, EPF-Lausanne, CH-1015 Switzerland.*

* *Previously publishing as Gelsomina De Stasio. Corresponding author: pupa@physics.wisc.edu*

Keywords: PIC, X-ray linear dichroism, crystal orientation, XANES, NEXAFS, X-PEEM, synchrotron, spectromicroscopy, Nacre, Abalone, Biomineral.

ABSTRACT. Many biominerals contain micro- or nano-crystalline mineral components, organized accurately into architectures that confer the material with improved mechanical performance at the macroscopic scale. We present here a new effect, which enables to observe the relative orientation of individual crystals at the sub-micron scale. We call it polarization-dependent imaging contrast (PIC), as it is an imaging development of the well-known x-ray linear dichroism. Most importantly PIC is obtained *in situ*, in pristine biominerals. We present here PIC in the prismatic and nacreous layers of *Haliotis rufescens* (red abalone), confirm it in geologic calcite and aragonite, and corroborate the experimental data with theoretical simulated spectra. PIC reveals new and unexpected aspects of nacre architecture that have inspired theoretical models for nacre formation.

INTRODUCTION. Nacre, or mother-of-pearl, is intensely studied by materials scientists, mineralogists, physicists as well as chemists, because of its remarkable mechanical properties and its fascinating and poorly understood formation (1,2). Nacre is a composite of layered 400-nm thick aragonite tablets (3), and 30-nm thick organic matrix layers (4,5). Aragonite, an orthorhombic $CaCO_3$ polymorph, is hard but brittle. Aragonite accounts for 95% of nacre's mass, leading one to expect the mechanical characteristics of nacre to be similar to those of aragonite, yet nacre is 3000 times more resistant to fracture than aragonite (6). Materials scientists have only recently began to learn how to prepare synthetic composites outperforming their components by such large factors, and do so inspired by nacre (7,8,9,10), although not as efficiently and orderly organized as natural nacre. It is therefore of extreme interest to understand and possibly harness the mechanisms of nacre formation. Here we report unprecedented observations on the structure and architecture of nacre enabled by the use of x-ray absorption near edge (XANES) spectroscopy (11), combined with PhotoElectron Emission spectroMicroscopy (X-PEEM)(12). These observations inform and inspire new theoretical models for nacre formation mechanisms (13).

We recently detected for the first time polarization-dependent contrast (PIC) in X-PEEM images of red abalone (*Haliotis rufescens*) nacre (13). Using X-PEEM, we observe that the intensities of two specific peaks, in the carbon and oxygen K-edge spectra, are anti-correlated. In the X-PEEM experiment the spectral peak intensities correspond to imaging pixel intensities, therefore PIC appears in real-time, full-field images. When detected in spectroscopy alone, without imaging, this effect is commonly referred to as x-ray linear dichroism, and it has been observed in magnetic materials (14,15), molecular chemisorbed systems (16), and liquid crystals (17). In carbonates, linearly polarized light provokes intense emission of specific peaks depending on the orientation of the carbonate crystal c-axis relative to the polarization vector[1] (18,19). If a complex biomineral containing multiple crystals is observed at once, the crystals with c-axes parallel and perpendicular to the polarization vector will appear white or black, respectively. Crystals with intermediate positions will appear with varying gray levels.

This effect, widely studied in the man-made systems mentioned above, has been observed in naturally occurring minerals (20,21), but has not been previously documented in a natural biomineral.

Here we comprehensively present the observation of polarization-dependent contrast with XANES spectra from red abalone shells, including the nacreous and prismatic layers. The latter comprises columns of the trigonal-rhombohedral $CaCO_3$ polymorph calcite. We also present XANES spectra from aragonite and calcite crystals, and show that they exhibit x-ray linear dichroism similar to that observed in the biomineral. We compare the data from crystals with simulated spectra and find good agreement between experimental and theoretical trends.

[1] The linear polarization vector is always in the synchrotron orbit plane, and is therefore horizontal.

Fully characterizing dichroism in calcite and aragonite enables us to study new aspects of biomineral structure *in situ*, in the pristine biomineral. We show here the first PIC images of the nacreous and the prismatic layers in abalone shells at the sub-micron, micron and millimeter scales. These results highlight the new capabilities afforded by PIC.

METHODS. Our minimally destructive X-PEEM experiments, probe a depth of ~3 nm at the C K-edge (Figure 1)(22), and can be done *in situ* in pristine biominerals as discussed in detail by Gilbert et al. (23,24). The only requirement is a flat surface for X-PEEM spectromicroscopy analysis, which is easily obtained by polishing.

We characterized PIC in red abalone by probing different regions within each shell, and multiple shells. Using the Spectromicroscope for the PHotoelectron Imaging of Nanostructures with X-rays (SPHINX) X-PEEM (12), samples were analyzed after embedding and polishing at different angles. PIC in SPHINX images guides navigation on the sample surfaces, identification of the nacre and prismatic layers, and localization of the boundary between them.

The geometry of the microscope is described extensively elsewhere (12). The parameter most relevant to the current experiments is the angle between the polarization vector in the illuminating light, and the c-axis of each crystal or micro-crystal. Soft-x-rays from either an undulator or bending magnet synchrotron source, are always polarized linearly and horizontally, that is, in the synchrotron orbit plane. Depending on the orientation of each crystal, its c-axis forms a different angle with respect to the polarization vector. Here, this angle is called θ, or the polar angle. In the SPHINX set-up the beam illuminates the sample at a grazing incidence angle of 16º, and the sample is always mounted vertically. The polarization vector, therefore, is always at 16º from the sample normal.

XANES spectra from geologic calcite and aragonite were acquired using two different chambers at two different synchrotrons: the XAB chamber at the SRC, installed on the HERMON beamline, and the AXIS chamber at the ALS on beamline 7.0.1. All of the C spectra for aragonite and calcite were acquired at ALS, all of the O spectra at SRC. In all cases the sample surface was maintained vertical, and the measurement was done in total electron yield. The polar dependence was obtained by changing the polar angle θ□□□□□□□□□□□□□□□□□□□□□□ for the two crystals. The aragonite and calcite crystals for C spectroscopy were polished so the c-axis was in plane. Polar variation was achieved rotating the aragonite sample position azimuthally, around the normal to its surface, while illuminating it with linearly polarized light. Similarly, the aragonite crystal for O spectroscopy had the c-axis in plane and was rotated azimuthally. The calcite crystal for O spectroscopy was cleaved so the c-axis was 40° from the sample surface normal. For calcite, polar variation was obtained by rotating the sample around a vertical axis. In the polar dependence curves the error bars are smaller for C than fopr O because the AXIS chamber is equipped with accurate azimuthal rotation on the sample manipulator, while the XAB chamber is not. For the latter the sample had to be inaccurately rotated via a transfer rod, leading to inferior repeatability.

Before analysis all crystals were characterized and oriented with x-ray diffraction, re-polished to remove the radiation-damaged surface, and cleaned three times in ultrasonic baths, with trichloroethane, acetone and ethanol, respectively, for 20 minutes each. They were then coated with Pt to improve conductivity.

RESULTS. In amorphous or unstructured samples, illumination with linearly polarized x-ray photons generates no contrast. In crystals, however, the intensity of specific peaks, associated with specific bonds, varies depending on the orientation of the polar angle. Because the prismatic and nacre layers of red abalone shells consist of calcite and aragonite micro-crystals, variation in crystalline orientation relative to the soft-x-ray beam generates imaging contrast: the PIC discussed here.

In Figure 2 we present the carbon, oxygen and calcium maps and spectra from a nacre sample surface.

The different gray levels in the carbon and oxygen maps of Figure 2 correspond to variations in the intensity of the 290.3[2] eV peak and 534 eV peak, which are the C1s→π* and O1s→π* transitions of the carbonate CO bond (hereafter called the π* peaks), and the 302 eV and 540 eV peaks, associated with the C1s→σ* and O1s→σ* transitions of the carbonate CO bond (σ* peaks). Immediately adjacent tablets exhibit strikingly strong contrast, as shown by the different gray levels, due to different orientations of adjacent crystalline tablets in each nacre layer. The π* and σ* peaks are anti-correlated, and exhibit the PIC or linear dichroism described above. Mapping these peaks yields PIC, as shown in Figure 2.

Calcium does not exhibit such contrast. This is interesting in view of a previous report that Ca in CaF_2 exhibits polarization dependence. That observation was due to breaking of the cubic symmetry at the CaF_2 surface (25). Our understanding is that PIC is bond-specific rather than element-specific. The lack of contrast in nacre calcium maps, therefore, is interesting, but not surprising.

Due to the lack of calcium PIC, Ca maps do not reveal individual tablets, and appear similar to images obtained with X-PEEM at energies away from π* and σ* peaks, or with any other microscopy technique.

The Ca spectra of Figure 2 show that the nacre regions examined, as expected, are aragonitic. Calcite and aragonite spectra are most distinct at the Ca L-edge in the energy ranges indicated by boxes in Figure 3. Peaks at these energies are assigned to crystal field resonance, which differs for different carbonates (25,26,27). The calcite and aragonite spectra at the Ca L-edge are shown in Figure 3.

[2] The carbonate peak position varies from sample to sample between 290.2 eV and 290.4 eV. We therefore report it here as 290.3 eV ± 0.1 eV. This should be considered the uncertainty for all other energies reported hereafter.

In Figure 4 we present X-PEEM data acquired on a cross-section of a prismatic layer. The growth direction is at 90º from the polarization vector.

The same PIC for the aragonitic nacre of Figure 2 is observed for C and O maps in Figure 4, revealing more than ten calcitic prismatic crystals. The Ca map, again, is homogenous and cannot distinguish different orientations in prismatic crystals.

As mentioned, PIC is the origin of the contrast observed in nacre tablets and prismatic crystals in Figures 2 and 4. To substantiate this observation we extended the analysis to simpler systems: geologic aragonite and calcite single crystals, as reported in Figures 5, 6 and 7. We clearly see that varying the polar angle θ dramatically changes the intensity of the π* and σ* peaks. Polar angle θ variation, therefore, is the origin of the contrast observed in Figures 2 and 4. In those cases the polarization vector and sample position were constant, while the orientation of adjacent crystallites varied.

PIC must arise from variations of the polar angle θ, between the c-axis of the crystal and the polarization vector, because the relative intensities of the peaks cannot vary when only the ab-plane angle is rotated around the c-axis (18), and aragonite has hexagonal symmetry in the ab-plane[3] (28).

The least manipulated data presentation for the polar dependence of C spectra is that used in Figures 5E and 7E, obtained directly from unnormalized raw spectra, and simply measuring the on-peak and off-peak intensity. For the off-peak intensity we selected the immediate pre-peak at 289.5 eV, as this leads to the least data scattering ion the polar plot. Since in the unnormalized raw data the spectral intensity varies dramatically, we report [I(π*)-I(pre-peak)]/I(pre-peak). For the oxygen spectra the π* peak is directly on the background, and not above the absorption edge as in C. Normalized or unnormalized spectra can therefore be used, and the off-peak energy is simply the pre-edge energy. In Figures 5F and 7F, we report I(π*)-I(pre-edge) from normalized spectra, as shown in the inset.

The polar dependence is evident in the raw data, as shown for example in the raw data of Figure 6. The π* peak intensity clearly reproduces the trend seen in the normalized data of Figure 5.

The experimental data of Figures 5-7 clearly reveal the polar dependence at the origin of the PIC effect. The polar dependence has a maximum at θ = 0° and minima at ±90°. A $\cos^2\theta$ dependence was predicted by theory, and observed in chemisorbed carbonate groups with XANES spectroscopy by Stöhr's group (18,19).

A detailed discussion of the peak observed at 285 eV is reported below in the appendix.

---

[3] Visualizing each carbonate group as a triangle, along one carbonate plane (ab-plane) all triangles are repeated identically. In the next carbonate plane, however, the triangles are rotated, so that two overlapping triangles describe a "star of David".

Simulations of the aragonite and calcite XANES spectra were done using the FEFF 8.2 software package (29) with an input file that used crystal coordinates for aragonite and calcite (28,30) and the POLARIZATION card to vary the polar angle θ. Both the experimental and the simulated spectra exhibit increase and decrease in the π* and σ* peak intensities, respectively, as the polar angle is decreased. Despite the lineshape inaccuracy of the simulated spectra, the anti-correlation of π* and σ* peaks is in good agreement with the experimental data.

In the raw data of the C and O PIC maps of Figure 2 we observe different intensities for the brightest and darkest tablets, as reported in Table 1.

Table 1

Map	Brightest tablet mean gray level	Darkest tablet mean gray level	Contrast range (brightest-darkest mean gray levels)
O map π*/σ*	179	72	107
O map π*/pre-edge	**223**	**31**	**192**
C map π*/σ*	**233**	**138**	**108**
C map π*/pre-edge	123	50	73

As expected, in Table 1 we observe that the π*/σ* maps exhibit the same contrast for C and O, since C and O are bonded to each other in carbonates. It is also clear, however, that the contrast is greater for the π*/σ* map for C and for the π*/pre-edge map for O (bold in Table 1). This is why in Figure 2 and all following figures from nacre and prismatic layer we reported these two maps.

An additional reason for selecting π*/σ* and π*/pre-edge for C and O maps, respectively, is that they do not emphasize spots of organic material in the sample and therefore do not muddy the signal from mineral crystals.

Having characterized the PIC effect in aragonite and calcite, we now use it to analyze the structure of nacre and prismatic crystals in red abalone non-destructively, by probing the relative crystallographic orientation of nacre tablets and prismatic crystals from the sub-micron to the millimeter scale.

In principle, the polar dependence curves presented at the end of Figures 5 and 7 could be used as calibration curves, to assign crystallographic orientation to the individual nacre tablets and prismatic crystals. However, further work is required to make PIC a rigorously quantitative measurement. Thus far, the maximum carbon [I(π*)-I(p˜peak)]/ I(p˜peak) for nacre is 0.88, which is well within the range observed for aragonite: up to 0.97. For prismatic crystals the maximum carbon [I(π*)-I(p˜peak)]/ I(p˜peak) measured was 0.48, which is well below the calcite maximum of 0.78, even without having reached the maximum at θ = 0°.

In principle, polar dependence curves similar to those of Figures 5E, 5F and 7E, 7F could be used as calibration curves to quantitatively measure the polar angle in C and O PIC maps of nacre and prismatic layer. In particular, a value for the polar angle θ could be assigned to each gray level in C and O maps, therefore measuring the crystallographic disorder in nacre tablets and prismatic crystals. In practice, however, a calibration curve must be obtained from nacre and prismatic layer directly, to ensure that the presence of organics or the small lattice distortions of biogenic aragonite in nacre, compared with geologic aragonite, observed by Pokroy et al. (31) do not induce significant differences in the π* peak intensities, and these behave in biogenic minerals as in geologic crystals. Accurate calibration curves similar to those presented here must be obtained from single nacre tablets and prismatic crystals to enable this quantitative analysis. Such data are extremely challenging to obtain, and will be subject of a future paper.

The O maps of Figure 8 show that PIC contrast in the prismatic layer does not change significantly with distance from the prismatic-nacre boundary. Due to the large crystal size, individual crystals and their orientation can be seen in visible light microscopy (VLM) using two crossed polarizer filters, one in the analysis channel and one in the illumination channel. Images acquired with the VLM confirm the observation that PIC in prismatic crystals is evident throughout the prismatic layer. In the nacre layer, however, the tablet crystals are too small and too transparent to be seen in cross-polarized VLM.

The C and Ca maps in Figure 9 show a high-resolution image of nacre tablets in cross-section. As seen previously, the C map shows PIC due to polar disorder in nacre tablets, while the Ca map does not show any dependence on crystal orientation. This high-contrast area was a few microns away from one of the nacre growth layers (32). The PIC gray level homogeneity within each tablet is consistent with previous reports that each tablet diffracts as a single crystal (33).

Surprisingly, the columns of co-oriented tablets start and end. A new tablet appears abruptly, as shown in all PIC maps acquired, and as represented in Figure 9.

In Figure 10 we present a series of O maps acquired with SPHINX at and away from the nacre-prismatic boundary, across the whole thickness of the nacre layer. The appearance of co-oriented nacre columns is unexpected and unprecedented. Specifically, thanks to the PIC in this figure, we observe that columns with several co-oriented tablets appear across nacre. The contrast observed in these maps is due to misorientation of the c-axes with respect to the polarization vector. Compared with the growth direction as well, the orientations of tablet c-axes differ from column to column. It is therefore incorrect to identify the growth direction of nacre with the c-axis, as is commonly done in the literature.

From the SPHINX results of Figure 10 and many others we see that the largest PIC occurs near the nacre-prismatic boundary. The contrast, corresponding to the degree of c-axis crystallographic disorder, quickly diminishes with the distance from the boundary. This is in agreement with previous observations by DiMasi and Sarikaya, using synchrotron x-ray micro-diffraction, that nacre tablets and prismatic crystals in red

abalone are less co-oriented near the nacre-prismatic boundary, and become more co-oriented and ordered within 100 μm of the boundary (34). This also agrees with the bulk XRD measurements taken by our group and others (33,35), which find that the a- and b-axes are randomly oriented while the c-axes of nacre tablets deviate from the growth direction by only ±11°. This is the footprint of the rocking curve, reported in Figure 11. We find that the maximum c-axis misorientation and PIC contrast is near the nacre-prismatic boundary, with a few exceptions. Occasionally, isolated regions away from the boundary exhibit extreme PIC. The data of Figure 2 were acquired in one such region. Lesser but still distinct PIC, however, is observed across the whole 2-mm thickness of the nacre layer, as seen in Figure 10.

DISCUSSION. We reported an extensive characterization of the PIC effect and its origin in the polarization-dependent spectral intensities in the nacreous and prismatic layers of red abalone, as well as single crystals of geologic aragonite and calcite. Theoretical simulations of the single crystal spectra are in good agreement with the experimental data. Combined, they fully explain the source of the contrast observed in red abalone shells.

It is interesting to notice that the values found for α, the maximum polar dependence value at $\theta = 0°$, for aragonite are 0.9 and 10 for C and O, and for calcite they are 1 and 10 for C and O, respectively. In each mineral, the difference between the C and O α values is not surprising. First of all the absorption cross-sections for C and O are different, second, the peak intensities measured are not the same. Due to the energy position of the π^* peak, which is above the C K-edge, and to the non-flat I_o at the C energies, the most accurate peak height is obtained subtracting an immediate pre-edge value, as shown in the insets of Figures 5 and 7. For O spectra, instead, the I_o is flat and the π^* is the lowest energy peak of the spectrum. This leads to a greater π^* and α values for O than for C, in both aragonite and calcite. Using normalized spectra for C (not shown) we obtained or $\alpha = 4.4$□□□□□□□□□□□□□□□□□□□□□□□□□□□□□□□□□□□□□,□□□□□□□□□□□□□□ □ In reasonable agreement with the result from raw data.

The reproducibility of the π^* and α values for C in aragonite and calcite (0.9 and 1), and those for O (10 and 10), is an important validation. This result is consistent with the fact that the carbonate groups are very similar in the structures of aragonite and calcite (28,30), therefore the CO bonds they form, which are detected by XANES spectroscopy, are also similar.

In this work we have initiated the use of PIC to study the nacreous and prismatic layers in red abalone. We have confirmed that there is greater variation in the nacre tablet orientation near the nacre-prismatic boundary. We have discovered that columns of co-oriented tablets appear in different gray levels, depending on tablet crystal orientation, and immediately adjacent columns may have completely different orientations. Unexpectedly and unprecedentedly, these columns of co-oriented tablets start and end abruptly. A possible explanation for this architecture relies on a specific formation mechanism for nacre, as described by Metzler et al. (13). In that simple static model,

nucleation sites are randomly distributed on pre-existing organic matrix layers, and co-orientation of tablets n+1 and n+2 is only possible if a nucleation site happens to be present between the two. A more sophisticated dynamic growth model is currently being developed. This will reveal which parameters are necessary and which ones ancillary to the formation of nacre in its specific architecture unraveled by PIC.

With the full body of data presented here as its solid foundation, the new PIC contrast mechanism can be used to investigate the structure and orientation of other polycrystalline systems and biominerals in particular, therefore revealing new and exciting architectures in pristine biominerals, and possibly inspire and inform new mechanisms for the formation of complex biominerals.

ACKNOWLEDGEMENTS. We are grateful to Ben Gilbert for his advice on FEFF simulations. This work was supported by NSF awards PHY-0523905 and CHE-0613972, UW-Graduate School Romnes and Vilas Awards to PUPAG, and NSF award DMR-0209630 to SNC. The experiments were performed at the UW-SRC, supported by NSF award DMR-0537588.

REFERENCES (to be shortened after the reviewing process)

1. Lowenstam, H.A.; Weiner, S. On Biomineralization. Oxford University Press, Oxford, **1989**.
2. Addadi, L.; Joester, D.; Nudelman, F.; Weiner, S.;. Mollusk Shell Formation: A Source of New Concepts for Understanding Biomineralization Processes. Chemistry Eur. J. 2006, 12, 980.
3. Mann, S. *Biomineralization*, Oxford University Press, New York, **2001**
4. Weiss, I.M. and Renner, C. and Strigl, M.G. and Fritz, M. A Simple and Reliable Method for the Determination and Localization of Chitin in Abalone Nacre. Chem. Mater. **2002**, *14*, 3252.
5. Rousseau, M. et al. Multiscale structure of sheet nacre. *Biomaterials* **2005**, 26, 6254-6262.
6. Currey, J.D. Mechanical Properties of Mother of Pearl in Tension. *Proc. R. Soc.Lond. B*. **1977**, *196*, 443.
7. Tang, Z. et al. *Nature Materials* **2003**, 2, 413-418.
8. Xu, G. and Yao, N. and Aksay, I.A. and Groves, J.T. Biomimetic Synthesis of Macroscopic-Scale Calcium Carbonate Thin Films. Evidence for a Multistep Assembly Process. *J. Am. Chem. Soc*. **1998**, *120*, 11977.
9. Wei, H. and Ma, N. and Shi, F. and Wang, Z. and Zhang, X. Artificial Nacre by Alternating Preparation of Layer-by-Layer Polymer Films and CaCO3 Strata. *Chem. Mater*. **2007**, *19*, 1974
10. Liu, X. Y.; Lim, S. W. Templating and Supersaturation-Driven Anti-Templating: Principles of Biomineral Architecture. *J. Am. Chem. Soc.* **2003**, 125, 888.
11. Stöhr, J. *NEXAFS Spectroscopy,* Springer-Verlag, Berlin, **1992**.

12. Frazer, B.H.; Girasole, M.; Wiese, L.M.; Franz, T.; De Stasio, G. Spectromicroscope for the Photoelectron Imaging of Nanostructures with X-rays (SPHINX): performance in biology, medicine and geology. *Ultramicroscopy,* **2004**, *99*, 87.
13. Metzler, R.A.; Abrecht, M.; Olabisi, R.M.; Ariosa, D.; Johnson, C.J.; Frazer, B.H.; Coppersmith, S.N.; Gilbert, P.U.P.A. Architecture of Columnar Nacre, and Implications for Its Formation Mechanism. *Phys. Rev. Lett.*, **2007**, *98*, 268102.
14. Roth, C.; Hillebrecht, F.U.; Rose, H.; Kisker, E. Linear magnetic dichroism in angular resolved Fe 3p core level photoemission *Phys. Rev. Lett.*, **1993**, *70*, 3479.
15. Stöhr, J.; Scholl, A.; Regan, T. J.; Anders, S.; Lüning, J.; Scheinfein, M. R.; Padmore, H. A.; White, R. L.; Images of the Antiferromagnetic Structure of a NiO(100) Surface by Means of X-Ray Magnetic Linear Dichroism Spectromicroscopy. *Phys. Rev. Lett.*, **1999**, *83*, 1862.
16. Stöhr, J.; Baberschke, K.; Jaeger, R.; Treichler, R.; Brennan, S. Orientation of chemisorbed molecules from surface-absorption fine-structure measurements: CO and NO on Ni(100). *Phys. Rev. Lett.,* **1981**, *47*, 381.
17. Stöhr, J.; Samant, M. G.; Lüning, J.; Callegari, A. C.; Chaudhari, P.; Doyle, J. P.; Lacey, J. A.; Lien, S. A.; Purushothaman, S.; Speidell, J. L.; Liquid Crystal Alignment on Carbonaceous Surfaces with Orientational Order. *Science*, **2001**, *292*, 2299.
18. Stöhr, J. *NEXAFS Spectroscopy,* Springer-Verlag, Berlin, **1992**.
19. Madix, R.J.; Solomon, J.L.; Stohr, J. The orientation of the carbonate anion on Ag(110). *Surface Science*, **1988**, *197*, L253.
20. van Aken, P. A.; Lauterbach, S. Strong magnetic linear dichroism in Fe L23 and O K electron energy-loss near-edge spectra of antiferromagnetic hematite a-Fe2O3. *Physics and Chemistry of Minerals*, **2003,** *30*, 469.
21. Templeton, D. H.; Templeton, L. K. Polarized Dispersion of X-rays in Pyrite. *Acta Cryst.*, **1997,** *A53,* 352.
22. Frazer, B.H.; Gilbert, B.; Sonderegger, B.R.; De Stasio, G. The probing depth of total electron yield in the sub- keV range: TEY-XAS and X-PEEM, *Surface Science*, **2003**, *537*, 161.
23. Gilbert, P.U.P.A.; Frazer, B.H.; Abrecht, M. In: *Molecular Geomicrobiology*. vol. 59 Mineralogical Society of America, Washington DC, 2005. p. 157-185, Banfield, J.F.; Nealson, K.H.; Cervini-Silva, J. (eds).
24. De Stasio, G., Frazer, B. H., Gilbert, B., Richter, K. L., Valley, J. W. Compensation of charging in X-PEEM: a successful test on mineral inclusions in 4.4 Ga old zircon. *Ultramicroscopy* **2003**, 98, 57.
25. Rieger, D.; Himpsel, F.J.; Karlsson, U.O.; McFeely, F.R.; Morar, J.F.; Yarmoff, J.A. Electronic structure of the CaF_2/Si(111) interface, *Phys. Rev. B.*, **1986**, *34*, 7295.
26. Naftel, S.J.; Sham, T.K.; Ylu, Y.M.; Yates, B.W. Calcium L-edge XANES study of some calcium compounds, *J. Synchrotron Rad.*, **2001**, *8*, 255.
27. Benzerara, K.; Yoon, T.H.; Tyliszczak, T.; Constantz, B.; Spormann, A.M.; Brown, G.E. Jr. Scanning transmission X-ray microscopy of microbial calcification. *Geobiology*, **2004**, *2*, 249.

28. Bevan, D.J.M.; Rossmanith, E.; Mylrea, D.K.; Ness, S.E.; Taylor, M.R.; Cuff, C. On the structure of aragonite- Lawrence Bragg revisited. *Acta Crystallographica,* **2002**, *B58*, 448.
29. Ankudinov, A.L.; Bouldin, C.; Rehr, J.J.; Sims, J.; Hung, H. Parallel calculation of electron multiple scattering using Lanczos algorithms. *Phys. Rev. B.*, **2002**, *65*, 104107.
30. Effenberger, E.; Mereiter, K; Zemann, J. Crystal structure refinements of magnesite, calcite, rhodochrosite, siderite, smithonite, and dolomite, with discussion of some aspects of the stereochemistry of calcite type carbonates. *Zeitschrift fur Kristallographie,* **1981**, *156*, 233.
31. Pokroy, B.; Quintana, J.P.; Caspi, E.N.; Berner, A.; Zolotoyabko, E. Anisotropic lattice distortions in biogenic aragonite, *Nature Materials*, **2004**, *3*, 900.
32. Su, X.; Belcher, A. M.; Zaremba, C. M.; Morse, D. E.; Stucky, G. D.; Heuer, A. H. Structural and microstructural characterization of the growth lines and prismatic microarchitecture in red abalone shell and the microstructures of abalone "flat pearl". *Chem. Mater.* **2002**, *14*, 3106.
33. Wise, S.W. Microarchitecture and mode of formation of nacre (mother-of-pearl) in pelecypods, gastropods, and cephalopods. *Eclogae Geol. Helv.*, **1970**, *63*, 775.
34. DiMasi, E.; Sarikaya, M. J. Synchrotron x-ray microbeam diffraction from abalone shell. *Mater Res.*, **2004**, *19*, 1471.
35. Zaremba, C.M.; Belcher, A.M.; Fritz, M.; Li, Y.; Mann, S.; Hansma, P.K.; Morse, D.E.; Speck, J.S.; Stucky, G.D. Critical Transition in the Biofabrication of Abalone Shells and Flat Pearls. *Chem. Mater.*, **1996**, *8*, 679.

APPENDIX

Detailed discussion of reference spectra

The aragonite cleaning procedure should have removed all adsorbed oils, humic substances and other contaminants, frequently present in geologic carbonates. In practice however, they were not sufficient to remove all contaminants, as shown by the presence of residual C peaks around 285 eV, typical of aromatic organic molecules. These peaks are not the result of radiation damage, and their intensity decreases with sample cleaning. The contaminant peaks at 285 eV do not overlap any of the carbonate peaks, therefore their presence does not affect any observation of the carbonate peaks discussed below. Interestingly, these peaks appear in geologic aragonite but not in calcite, at least in the crystals studied here. In spectra from abalone shells they do not appear in the aragonitic nacre, and do appear in the calcitic prismatic layer. Data in nacre and prismatic layers were also acquired at doses far below the onset of damage. Therefore this result may indicate differences in the proteins present in these two biominerals, with greater concentration of C=C double bonds in the prismatic than in the nacre layer.

FIGURE CAPTIONS

Figure 1. The escape depth of secondary photoelectrons at the C K-edge is ~3 nm, therefore only one layer of nacre tablets or prismatic crystals at a time is probed. The curve is an exponential fit to the experimental data points. Data adapted from Frazer et al. (22).

Figure 2. (**A**) Carbon π*/σ* map of the polished surface of red abalone nacre, showing polarization dependent contrast (PDC). The map was obtained by digital ratio of two SPHINX micrographs, acquired at 290.3 and 302 eV, respectively the π* and σ* peak energies shown in (B). The immediately adjacent tablets labeled 1 and 5 exhibit the highest contrast. Different gray levels correspond to different crystal orientations. (**B**) Carbon spectra extracted from the correspondingly labeled regions in (A). The intensities of the π* and σ* peaks are anti-correlated and vary dramatically from tablet to tablet, generating the contrast seen in (A), which in turn depends on crystal orientation and polarization. These and all other C spectra were normalized to a beamline background, and then to a linear fit above 310 eV, so that the spectral intensities below 283 eV and above 310 eV are 0 and 1, respectively. **(C)** Oxygen map obtained by digital ratio of images at 534 and 531.7 eV, the π* and pre-edge energies, respectively. (**D**) Oxygen spectra from the same regions, reproducing the anti-correlation of the π* and σ* peaks seen for carbon. All O spectra were normalized to a beamline background, and then linear fit above 555 eV so that spectral intensities below 530 eV and above 555 eV are 0 and 1, respectively. (**E**) Calcium map of the same nacre area, obtained by digital ratio of images at 352.7 and 343.7 eV. This map represents only a distribution map, showing much greater Ca concentration in the tablet compared to the organic matrix layers separating them. The polarization dependence observed in (A) and (C) is not detected in this map. (**F**) Calcium spectra extracted from the regions labeled in (A)**,** show that all regions examined are aragonite. All Ca spectra were normalized to a linear background, representative of the beamline background, and then linear fit above 355 eV so that spectral intensities below 346 eV and above 355 eV are 0 and 1 respectively. The nacre growth direction of this sample is perpendicular to the sample surface, therefore, the organic matrix layers are parallel to the sample surface. As they are not perfectly flat they appear as contour lines.

Figure 3. Aragonite (A) and calcite (B) Ca L-edge XANES spectra acquired on geologic aragonite and calcite crystals (red curves). These spectra are dramatically different in the crystal field resonance regions highlighted by the gray boxes. They are however very similar to the spectra of nacre and prismatic crystals respectively (black curves).

Figure 4. (**A**) Carbon π*/σ*map from the surface of a polished cross-section of red abalone prismatic layer. (**B**) Carbon K-edge XANES spectra extracted from the correspondingly labeled regions in (A) exhibit anti-correlated intensity of the π* and σ* peaks. **(C)** Oxygen map of the π*/pre-edge signal at 534 and 528 eV, respectively. (**D**) Oxygen K-edge XANES spectra. (**E**) Calcium distribution map of the same prismatic region, obtained by a digital ratio of images acquired at 351.4 (on the calcite peak) and

344.4 eV. (**F**) Calcium L-edge XANES spectra extracted from regions labeled in (**A**), showing that all regions examined are calcite.

Figure 5. (**A**) Carbon spectra acquired from a single geologic aragonite crystal as the polar angle θ was varied. Only a subset of the spectra were displayed and offset for clarity. (**B**) FEFF simulated C spectra for aragonite at different polar angles. While the lineshape does not accurately portray the experimental data, the anti-correlation between the π* and σ* peaks is consistent between the experimental and simulated spectra. (**C**) Oxygen spectra from another single crystal of aragonite. (**D**) FEFF simulated O spectra. (**E**) Polar dependence (black dots) of the π* peak, obtained by measuring, in the raw data of Figure 6 and others, the intensities at 290.3 eV and 289.5 eV. These are the π* peak and the immediate pre-peak intensity, respectively, shown in the inset. Due to intensity variations in the unnormalized data, each of the π* peak intensities had to be scaled to its pre-peak intensity. The parameter displayed, therefore, is not I(π*)-I(pre-peak) but [I(π*)-I(pre-peak)]/I(pre-peak). A direct measurement of the error bars was obtained from three repeated acquisitions returning to θ = -11° and θ = 22°. Theory predicts a variation of the π* intensity with a $\cos^2\theta$ dependence (13,14). A fit of the experimental data (red curve) reveals that the dependence is indeed [I(π*)-I(pre-peak)]/ I(pre-peak) = $\alpha\cos^2\theta$. The fit parameter α is 0.9 for carbon in aragonite. (**F**) The polar dependence for the normalized oxygen spectra in (C), and I(π*)-I(pre-edge) = $\alpha\cos^2\theta$ fit (red curve), with α = 10 for O in aragonite.

Figure 6. (**A**) Selected raw data XANES spectra acquired at different polar angles. Even in these raw data the decrease of π* peak intensity with θ is evident. Again only selected spectra are shown for clarity. The only processing here was vertical displacement and scaling, necessary because the spectra had wide variations in intensity. The black curve, labeled I_o, is the beamline background curve, acquired simultaneously with the θ = 0° spectrum. Each of the spectra in Figure 5A was normalized to a different I_o, simultaneously acquired. The polar variation of Figure 5E was obtained from these and many other spectra.

Figure 7. (**A**) Carbon spectra of a single crystal of geologic calcite at different polar angles. (**B**) FEFF simulated carbon spectra of calcite. Oxygen experimental (**C**) and simulated (**D**) spectra. (**E**) Carbon and (**F**) oxygen polar dependences data (black dots) and fit (red curves). Again the two data points at θ = 90° for C and θ = -10° for O indicate the experimental uncertainty. As in Figure 5, we report [I(π*)-I(pre-peak)]/ I(pre-peak) for C and [I(π*)-I(pre-edge)] for O spectra. As for aragonite, also for calcite an acceptable fit is obtained by $\alpha\cos^2\theta$, with α = 1 for carbon and α = 10 for oxygen.

Figure 8. (**A**) Composite visible light microscopy (VLM) images of a polished cross-section of red abalone, acquired in differential interference contrast mode. The green circles indicate prismatic areas examined with SPHINX. (**B**) A series of π*/pre-edge O maps of the areas shown in (A). (**C**) VLM image taken with crossed polarizers on the same red abalone shell. The prismatic crystals appear on top in various shades of brown, the nacre is cyan, at the bottom.

Figure 9. Single-energy SPHINX image at 344 eV, carbon and calcium maps, taken at the nacre-prismatic boundary of a piece of polished red abalone. The carbon π*/σ* map is the ratio of two images taken at 290.3 and 302 eV, respectively, and the calcium map is the ratio of 352 and 344 eV images. In this 90° cross-section the growth direction was in plane, at 74° from the polarization vector. Notice the PDC imaging contrast in the carbon map, while the direct image and the Ca map do not show any contrast. Dark Ca-poor spots in the Ca map appear at the sides of each tablet, where organics were located.

Figure 10. (**A**) Visible light microscopy composite micrographs of a polished section of red abalone shell, acquired in differential interference contrast mode. The nacre growth direction was 30° from the sample surface normal. The line between two magenta arrowheads is the prismatic-nacre boundary. The black rectangles outline the areas in which the O maps in (B) were acquired with SPHINX. (**B**) Series of oxygen PIC maps, obtained by digital ratio of images acquired at 534 and 530 eV, π* and pre-edge, respectively. PIC is clearly detectable across the entire thickness of the nacre layer. The central PIC map was acquired across one of the vertical lines evident in the optical image, which do not appear to affect tablet order or contrast. To enhance contrast in bulk nacre all raw grayscale maps were leveled and converted to a blue quadtone.

Figure 11. (**A**) X-ray diffraction pole figure indicates random orientation of nacre tablets in the ab-plane. (**B**) Rocking curve taken on the (002) Bragg peak on a piece of red abalone nacre. The 22º footprint of the rocking curve indicates that the c-axis variation in bulk nacre varies by ±11º, with instrument resolution better than 0.1º.

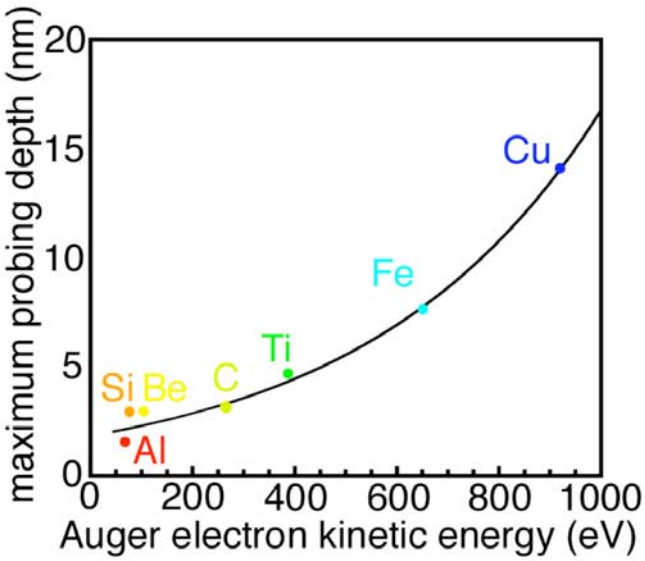

Figure 1. The escape depth of secondary photoelectrons at the C K-edge is ~3 nm, therefore only one layer of nacre tablets or prismatic crystals at a time is probed. The curve is an exponential fit to the experimental data points. Data adapted from Frazer et al. (17).

Figure 2

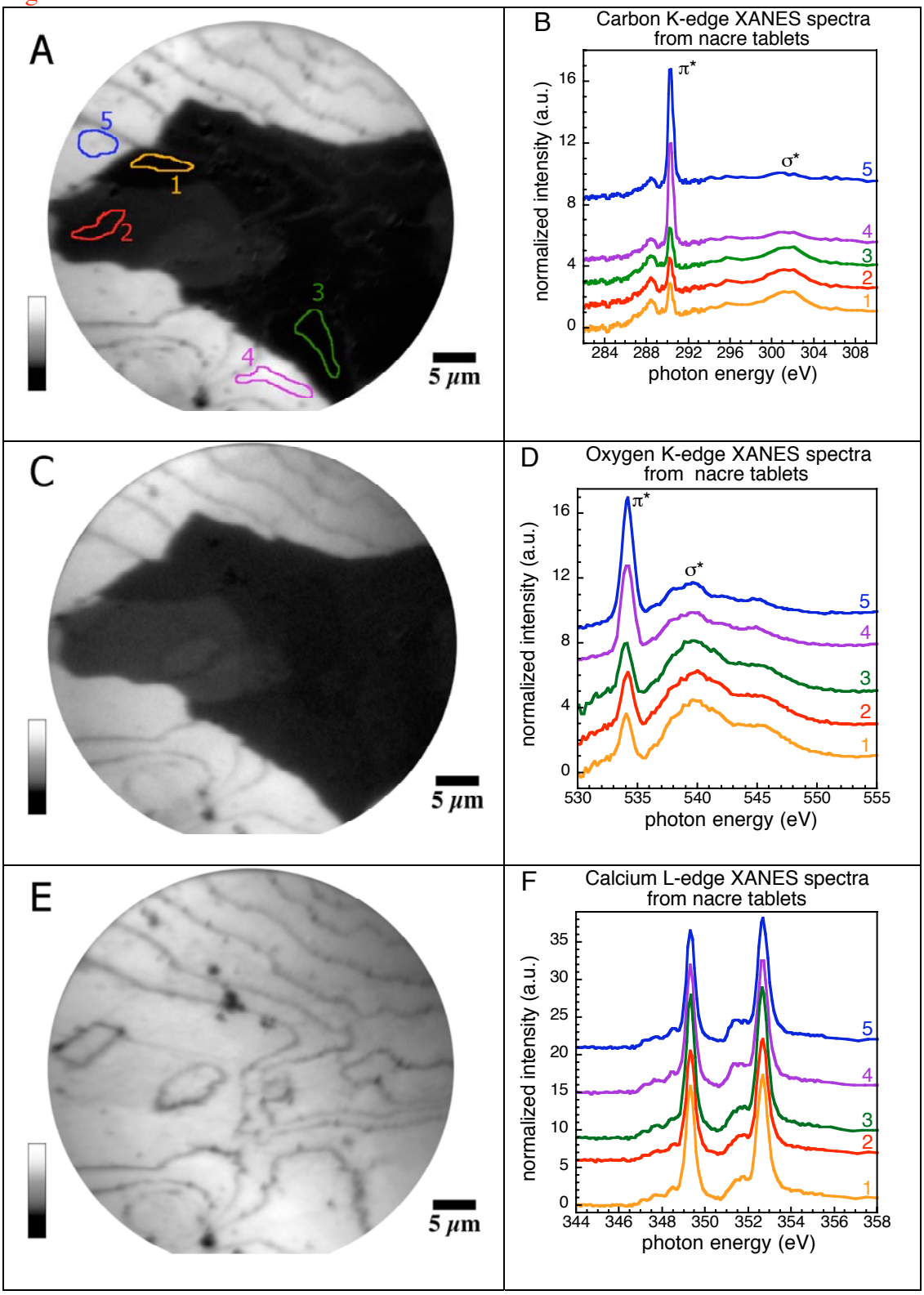
A
5
1
2
3
4
5 μm
B
Carbon K-edge XANES spectra
from nacre tablets
π*
σ*
normalized intensity (a.u.)
0
4
8
12
16
284 288 292 296 300 304 308
photon energy (eV)
C
5 μm
D
Oxygen K-edge XANES spectra
from nacre tablets
π*
σ*
normalized intensity (a.u.)
0
4
8
12
16
530 535 540 545 550 555
photon energy (eV)
E
5 μm
F
Calcium L-edge XANES spectra
from nacre tablets
normalized intensity (a.u.)
0
5
10
15
20
25
30
35
344 346 348 350 352 354 356 358
photon energy (eV)

Figure 2. (**A**) Carbon π*/σ* map of the polished surface of red abalone nacre, showing polarization dependent contrast (PDC). The map was obtained by digital ratio of two SPHINX micrographs, acquired at 290.3 and 302 eV, respectively the π* and σ* peak energies shown in (B). The immediately adjacent tablets labeled 1 and 5 exhibit the highest contrast. Different gray levels correspond to different crystal orientations. (**B**) Carbon spectra extracted from the correspondingly labeled regions in (A). The intensities of the π* and σ* peaks are anti-correlated and vary dramatically from tablet to tablet, generating the contrast seen in (A), which in turn depends on crystal orientation and polarization. These and all other C spectra were normalized to a beamline background, and then to a linear fit above 310 eV, so that the spectral intensities below 283 eV and above 310 eV are 0 and 1, respectively. **(C)** Oxygen map obtained by digital ratio of images at 534 and 531.7 eV, the π* and pre-edge energies, respectively. (**D**) Oxygen spectra from the same regions, reproducing the anti-correlation of the π* and σ* peaks seen for carbon. All O spectra were normalized to a beamline background, and then linear fit above 555 eV so that spectral intensities below 530 eV and above 555 eV are 0 and 1, respectively. (**E**) Calcium map of the same nacre area, obtained by digital ratio of images at 352.7 and 343.7 eV. This map represents only a distribution map, showing much greater Ca concentration in the tablet compared to the organic matrix layers separating them. The polarization dependence observed in (A) and (C) is not detected in this map. (**F**) Calcium spectra extracted from the regions labeled in (A)**,** show that all regions examined are aragonite. All Ca spectra were normalized to a linear background, representative of the beamline background, and then linear fit above 355 eV so that spectral intensities below 346 eV and above 355 eV are 0 and 1 respectively. The nacre growth direction of this sample is perpendicular to the sample surface, therefore, the organic matrix layers are parallel to the sample surface. As they are not perfectly flat they appear as contour lines.

Figure 3

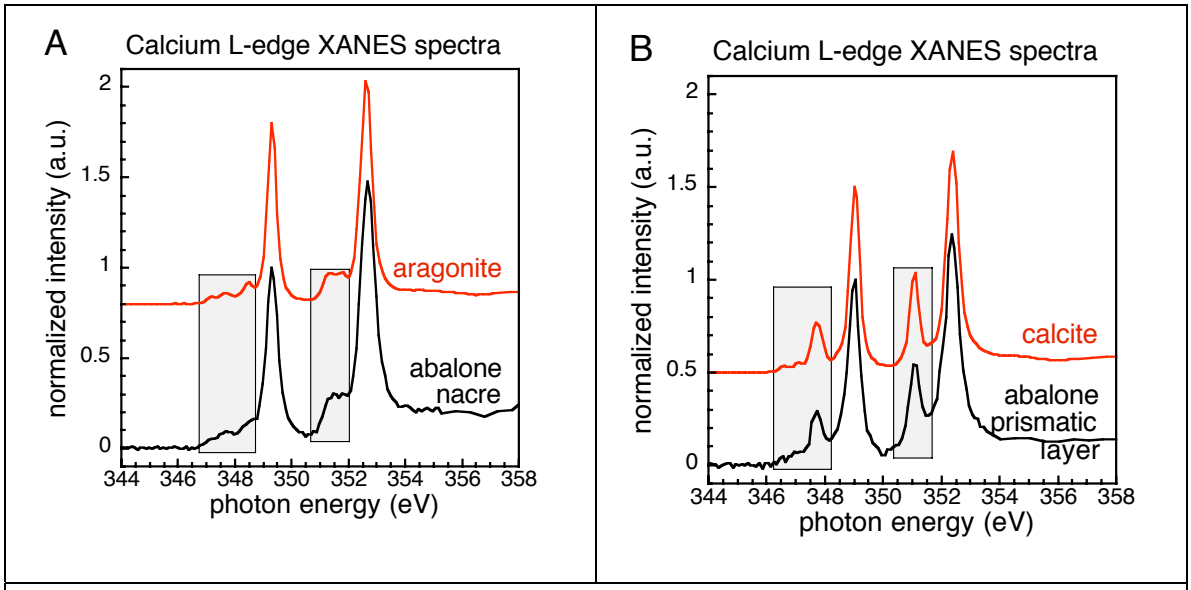

Figure 3. Aragonite (A) and calcite (B) Ca L-edge XANES spectra acquired on geologic aragonite and calcite crystals (red curves). These spectra are dramatically different in the crystal field resonance regions highlighted by the gray boxes. They are however very similar to the spectra of nacre and prismatic crystals respectively (black curves).

Figure 4

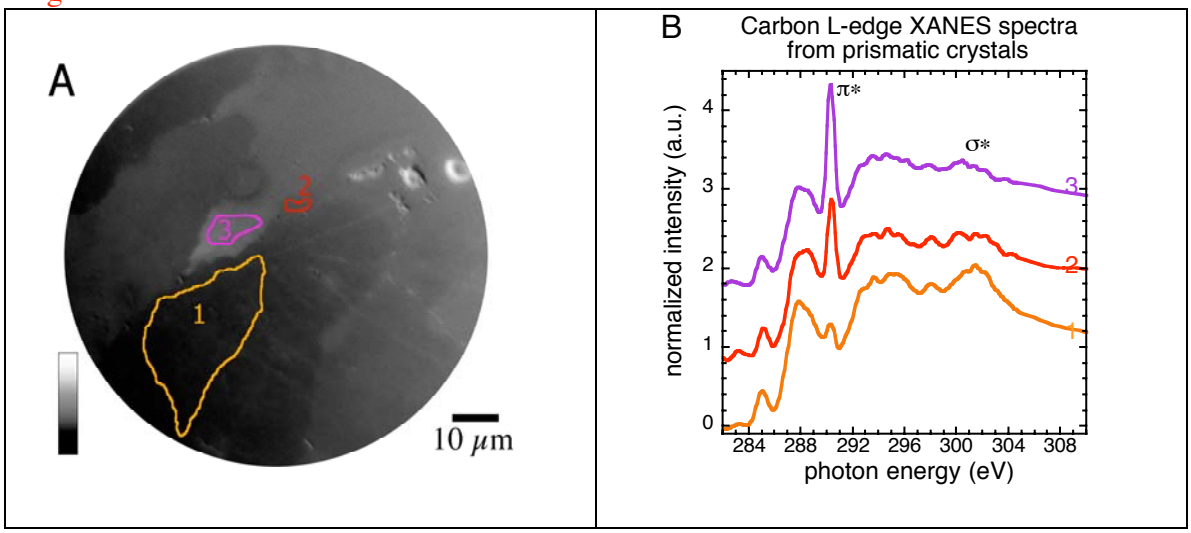

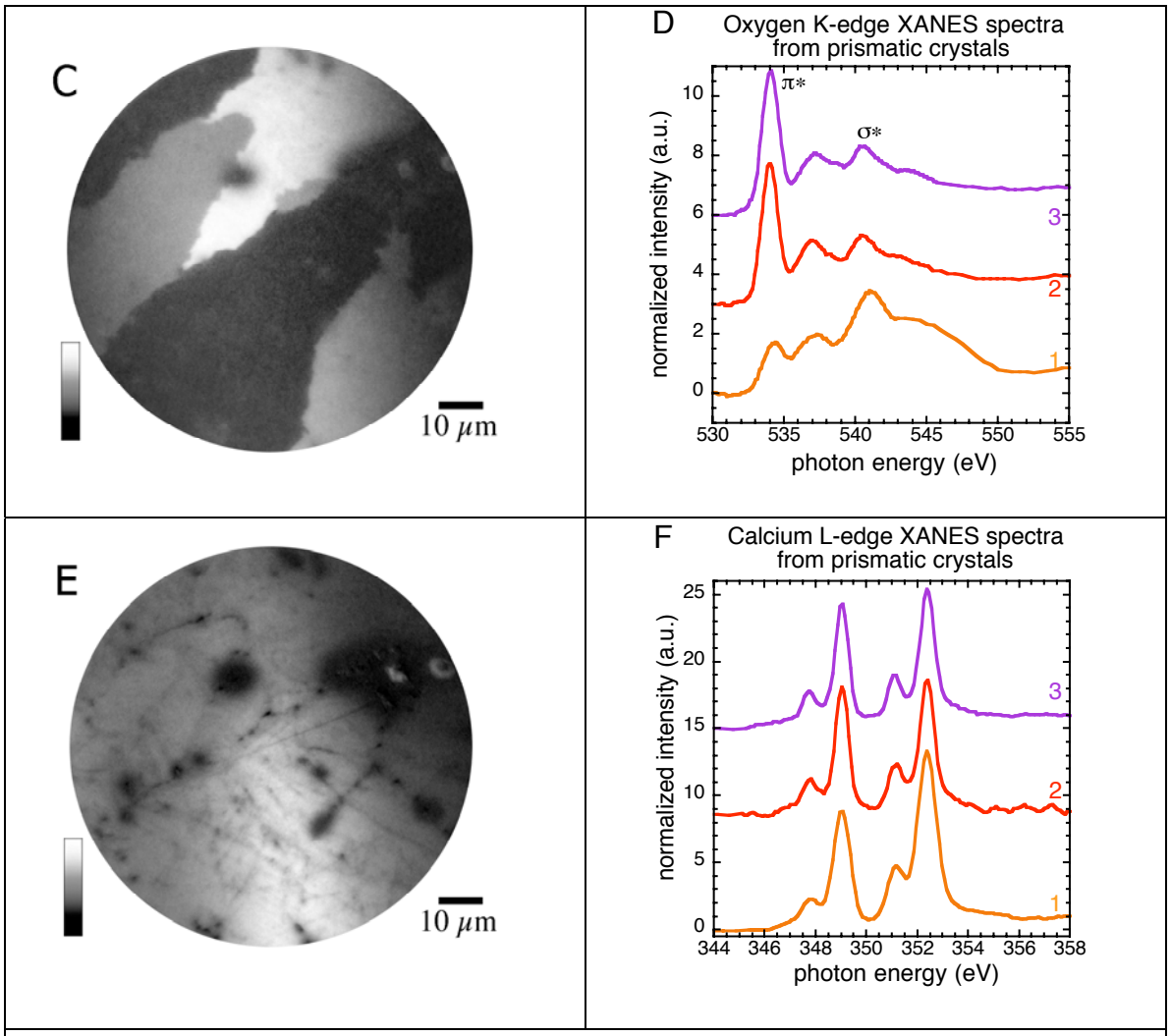

Figure 4. (**A**) Carbon π*/σ*map from the surface of a polished cross-section of red abalone prismatic layer. (**B**) Carbon K-edge XANES spectra extracted from the correspondingly labeled regions in (A) exhibit anti-correlated intensity of the π* and σ* peaks. **(C)** Oxygen map of the π*/pre-edge signal at 534 and 528 eV, respectively. (**D**) Oxygen K-edge XANES spectra. (**E**) Calcium distribution map of the same prismatic region, obtained by a digital ratio of images acquired at 351.4 (on the calcite peak) and 344.4 eV. (**F**) Calcium L-edge XANES spectra extracted from regions labeled in (**A**)**,** showing that all regions examined are calcite.

Figure 5

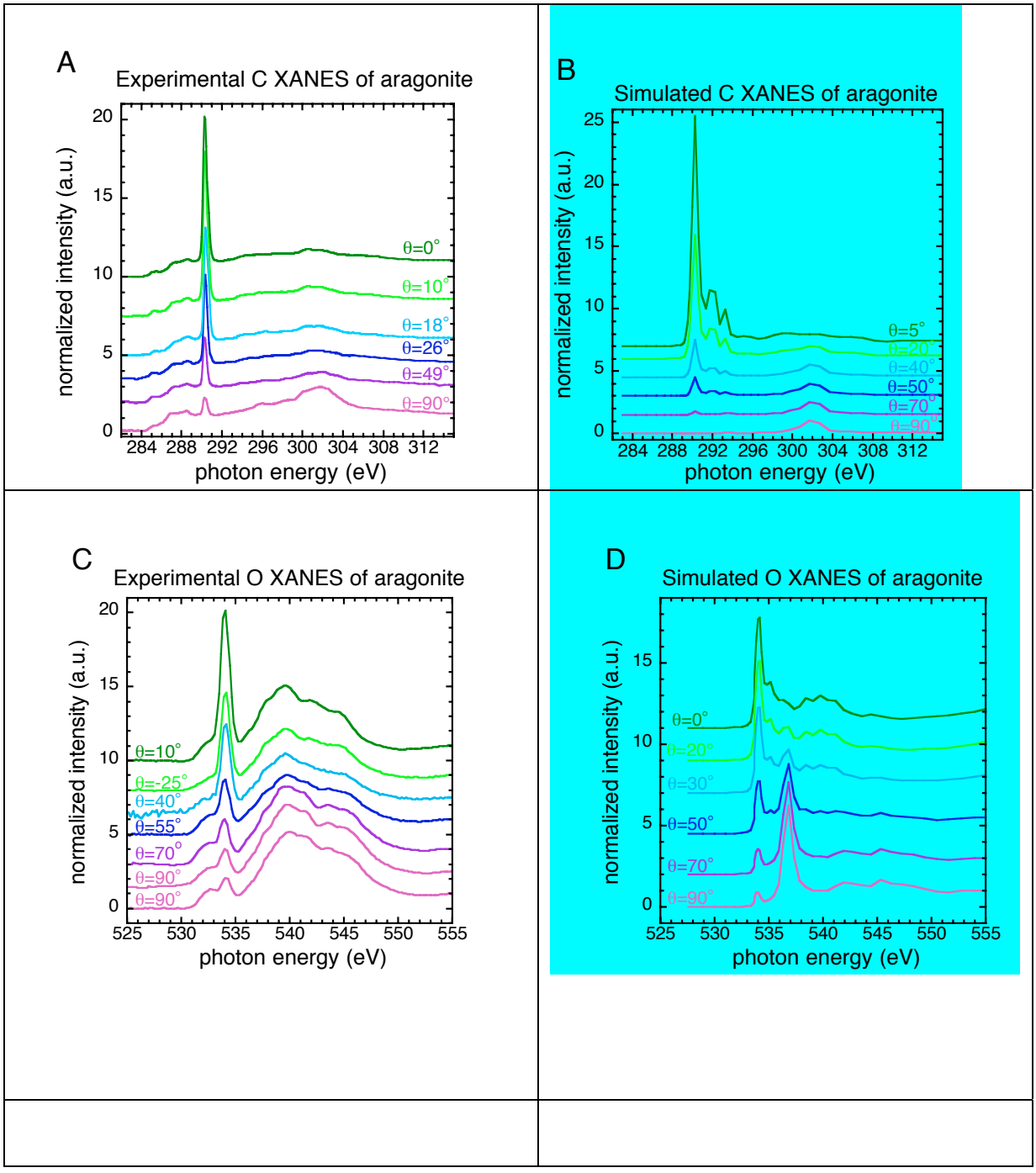
A
Experimental C XANES of aragonite
normalized intensity (a.u.)
photon energy (eV)
θ=0°
θ=10°
θ=18°
θ=26°
θ=49°
θ=90°
B
Simulated C XANES of aragonite
normalized intensity (a.u.)
photon energy (eV)
θ=5°
θ=20°
θ=40°
θ=50°
θ=70°
θ=90°
C
Experimental O XANES of aragonite
normalized intensity (a.u.)
photon energy (eV)
θ=10°
θ=-25°
θ=40°
θ=55°
θ=70°
θ=90°
θ=90°
D
Simulated O XANES of aragonite
normalized intensity (a.u.)
photon energy (eV)
θ=0°
θ=20°
θ=30°
θ=50°
θ=70°
θ=90°

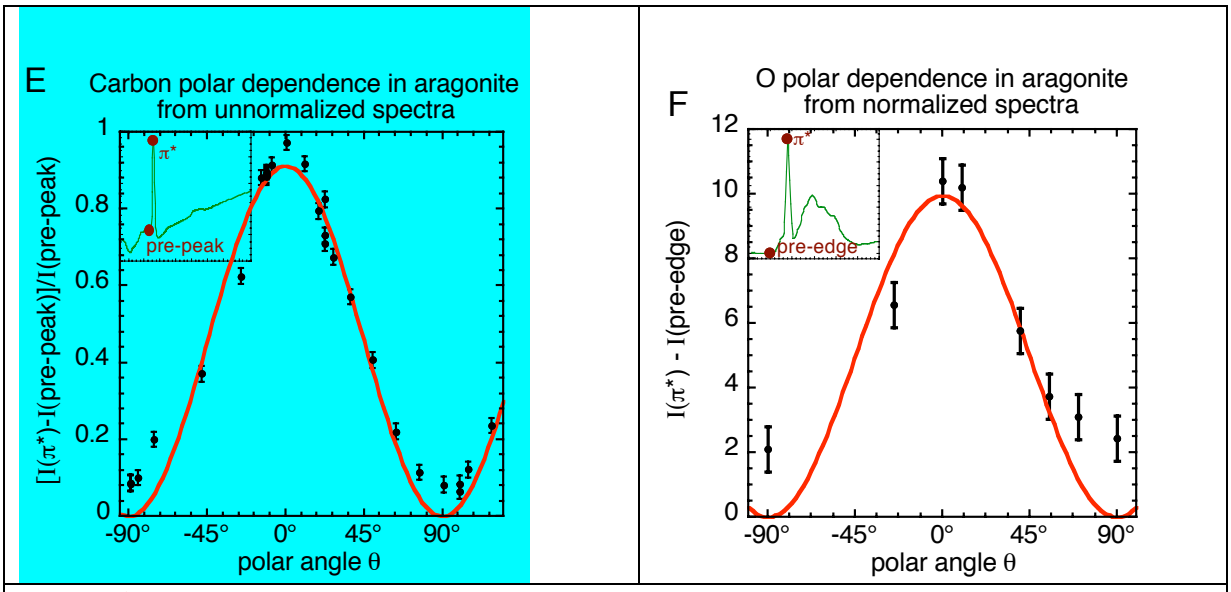

Figure 5. (**A**) Carbon spectra acquired from a single geologic aragonite crystal as the polar angle θ was varied. Only a subset of the spectra were displayed and offset for clarity. (**B**) FEFF simulated C spectra for aragonite at different polar angles. While the lineshape does not accurately portray the experimental data, the anti-correlation between the π* and σ* peaks is consistent between the experimental and simulated spectra. (**C**) Oxygen spectra from another single crystal of aragonite. (**D**) FEFF simulated O spectra. (**E**) Polar dependence (black dots) of the π* peak, obtained by measuring, in the raw data of Figure 6 and others, the intensities at 290.3 eV and 289.5 eV. These are the π* peak and the immediate pre-peak intensity, respectively, shown in the inset. Due to intensity variations in the unnormalized data, each of the π* peak intensities had to be scaled to its pre-peak intensity. The parameter displayed, therefore, is not I(π*)-I(pre-peak) but [I(π*)-I(pre-peak)]/I(pre-peak). A direct measurement of the error bars was obtained from three repeated acquisitions returning to θ = -11° and θ = 22°. Theory predicts a variation of the π* intensity with a $\cos^2\theta$ dependence (13,14). A fit of the experimental data (red curve) reveals that the dependence is indeed [I(π*)-I(pre-peak)]/ I(pre-peak) = $\alpha\cos^2\theta$. The fit parameter α is 0.9 for carbon in aragonite. (**F**) The polar dependence for the normalized oxygen spectra in (C), and I(π*)-I(pre-edge) = $\alpha\cos^2\theta$ fit (red curve), with α = 10 for O in aragonite.

Figure 6

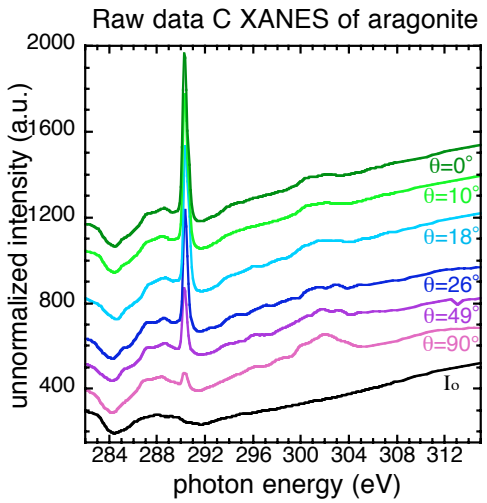

Figure 6. (**A**) Selected raw data XANES spectra acquired at different polar angles. Even in these raw data the decrease of π* peak intensity with θ is evident. Again only selected spectra are shown for clarity. The only processing here was vertical displacement and scaling, necessary because the spectra had wide variations in intensity. The black curve, labeled I_o, is the beamline background curve, acquired simultaneously with the θ = 0° spectrum. Each of the spectra in Figure 5A was normalized to a different I_o, simultaneously acquired. The polar variation of Figure 5E was obtained from these and many other spectra.

Figure 7

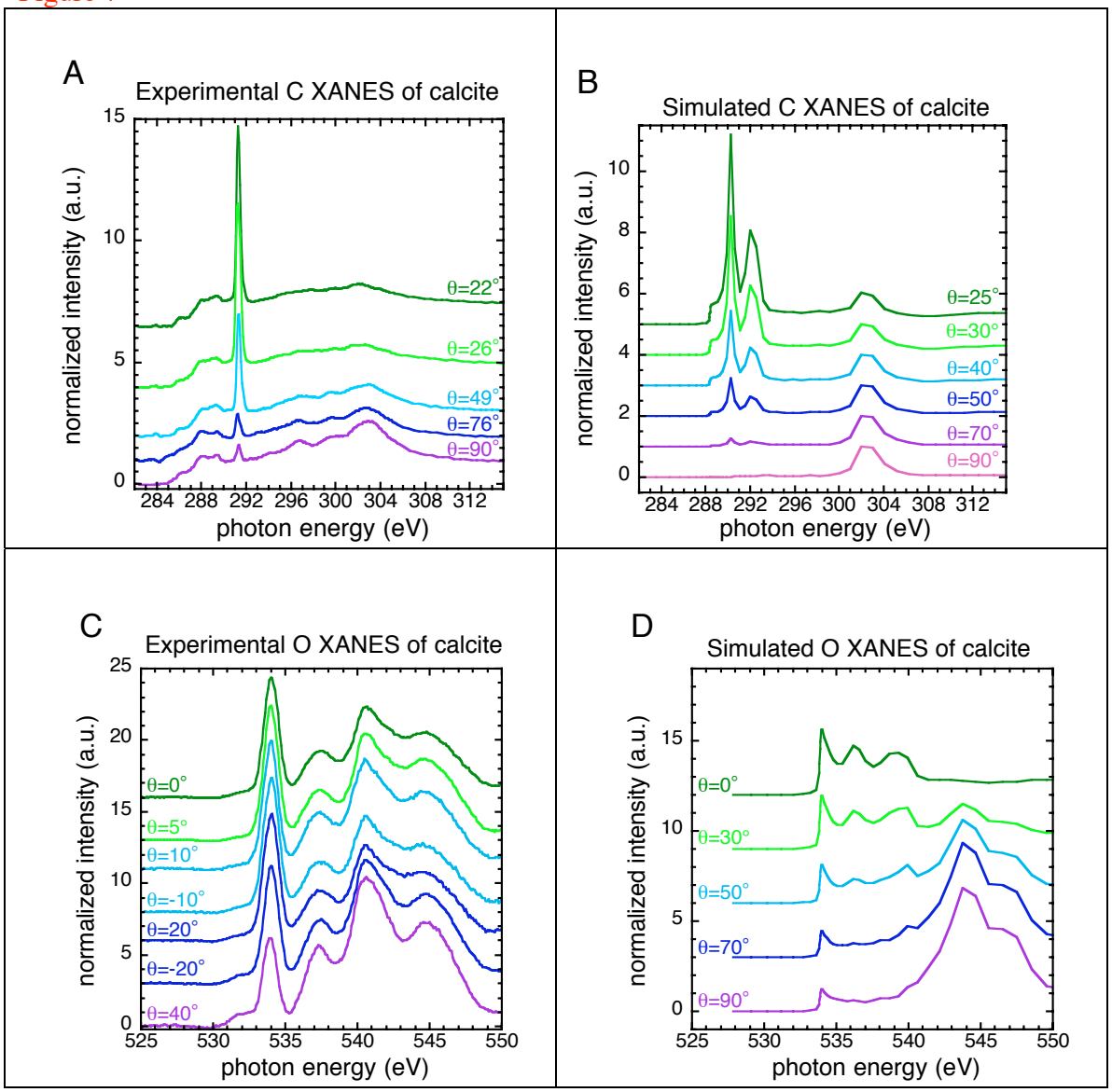
A
Experimental C XANES of calcite
normalized intensity (a.u.)
photon energy (eV)
θ=22°
θ=26°
θ=49°
θ=76°
θ=90°
B
Simulated C XANES of calcite
normalized intensity (a.u.)
photon energy (eV)
θ=25°
θ=30°
θ=40°
θ=50°
θ=70°
θ=90°
C
Experimental O XANES of calcite
normalized intensity (a.u.)
photon energy (eV)
θ=0°
θ=5°
θ=10°
θ=-10°
θ=20°
θ=-20°
θ=40°
D
Simulated O XANES of calcite
normalized intensity (a.u.)
photon energy (eV)
θ=0°
θ=30°
θ=50°
θ=70°
θ=90°

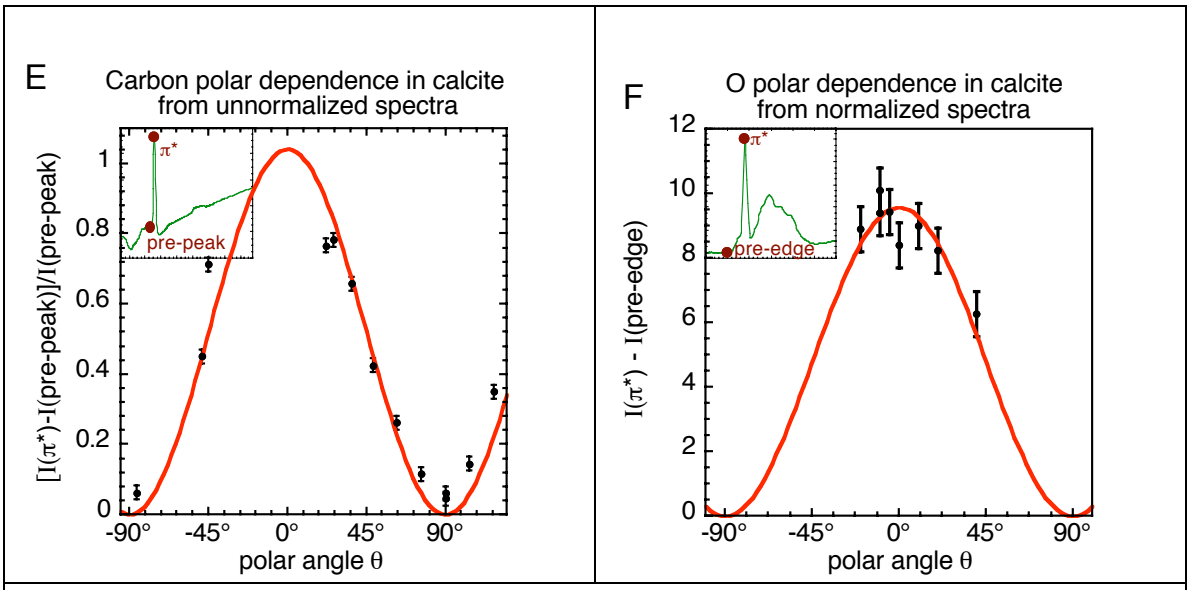

Figure 7. (**A**) Carbon spectra of a single crystal of geologic calcite at different polar angles. (**B**) FEFF simulated carbon spectra of calcite. Oxygen experimental (**C**) and simulated (**D**) spectra. (**E**) Carbon and (**F**) oxygen polar dependences data (black dots) and fit (red curves). Again the two data points at $\theta = 90°$ for C and $\theta = -10°$ for O indicate the experimental uncertainty. As in Figure 5, we report [I(π*)-I(pre-peak)]/ I(pre-peak) for C and [I(π*)-I(pre-edge)] for O spectra. As for aragonite, also for calcite an acceptable fit is obtained by $\alpha\cos^2\theta$, with $\alpha = 1$ for carbon and $\alpha = 10$ for oxygen.

Figure 8

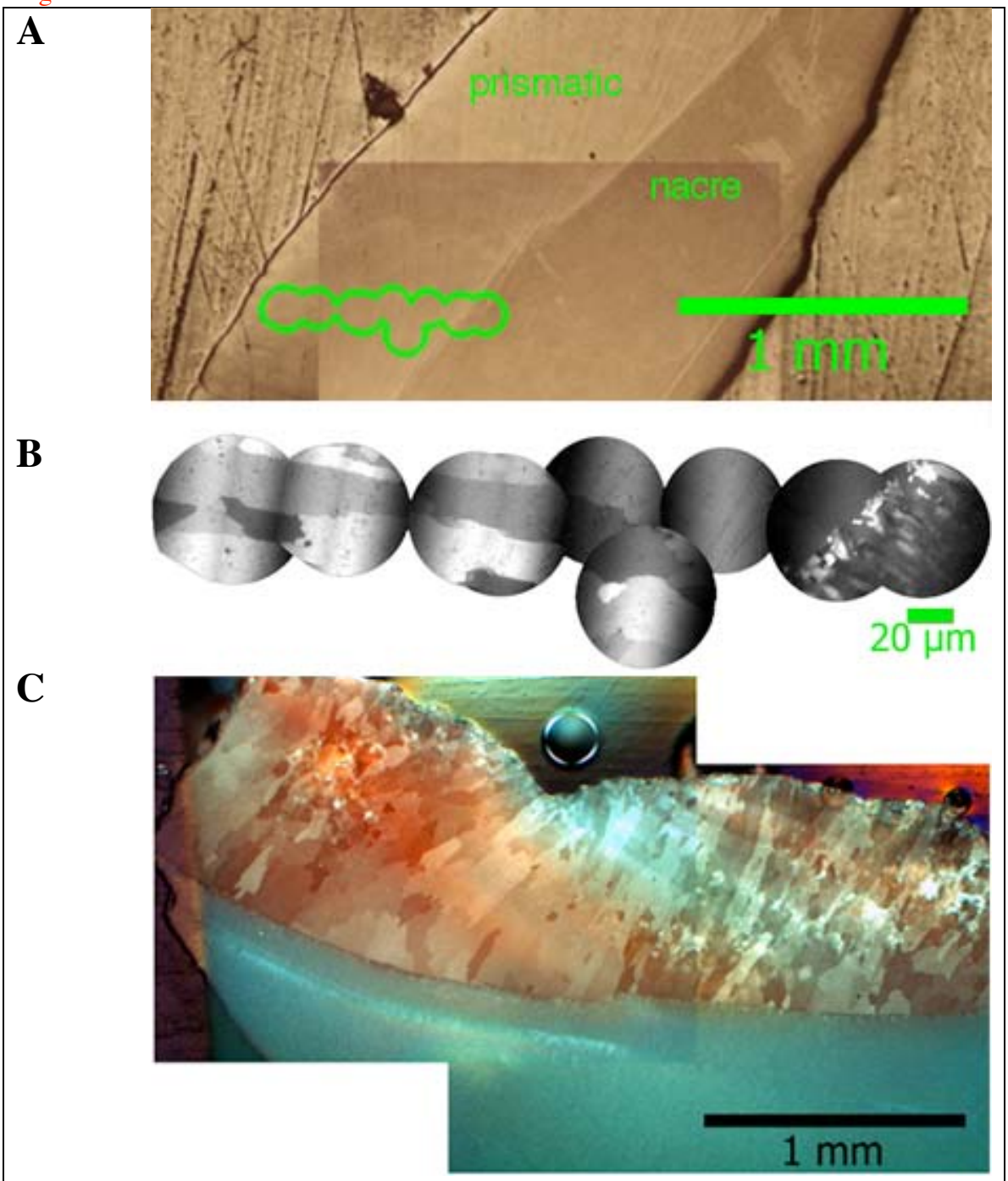

Figure 8. (**A**) Composite visible light microscopy (VLM) images of a polished cross-section of red abalone, acquired in differential interference contrast mode. The green circles indicate prismatic areas examined with SPHINX. (**B**) A series of π*/pre-edge O maps of the areas shown in (A). (**C**) VLM image taken with crossed polarizers on the same red abalone shell. The prismatic crystals appear on top in various shades of brown, the nacre is cyan, at the bottom.

Figure 9

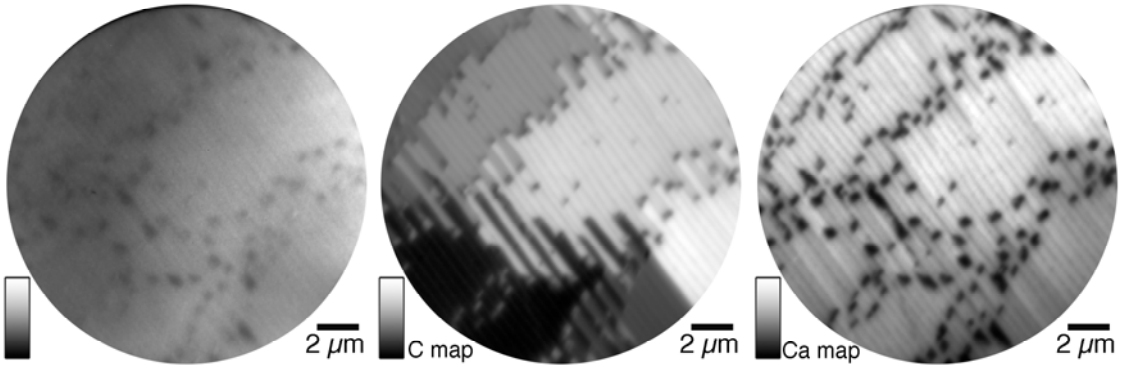

Figure 9. Single-energy SPHINX image at 344 eV, carbon and calcium maps, taken at the nacre-prismatic boundary of a piece of polished red abalone. The carbon π*/σ* map is the ratio of two images taken at 290.3 and 302 eV, respectively, and the calcium map is the ratio of 352 and 344 eV images. In this 90° cross-section the growth direction was in plane, at 74° from the polarization vector. Notice the PDC imaging contrast in the carbon map, while the direct image and the Ca map do not show any contrast. Dark Ca-poor spots in the Ca map appear at the sides of each tablet, where organics were located.

Figure 10

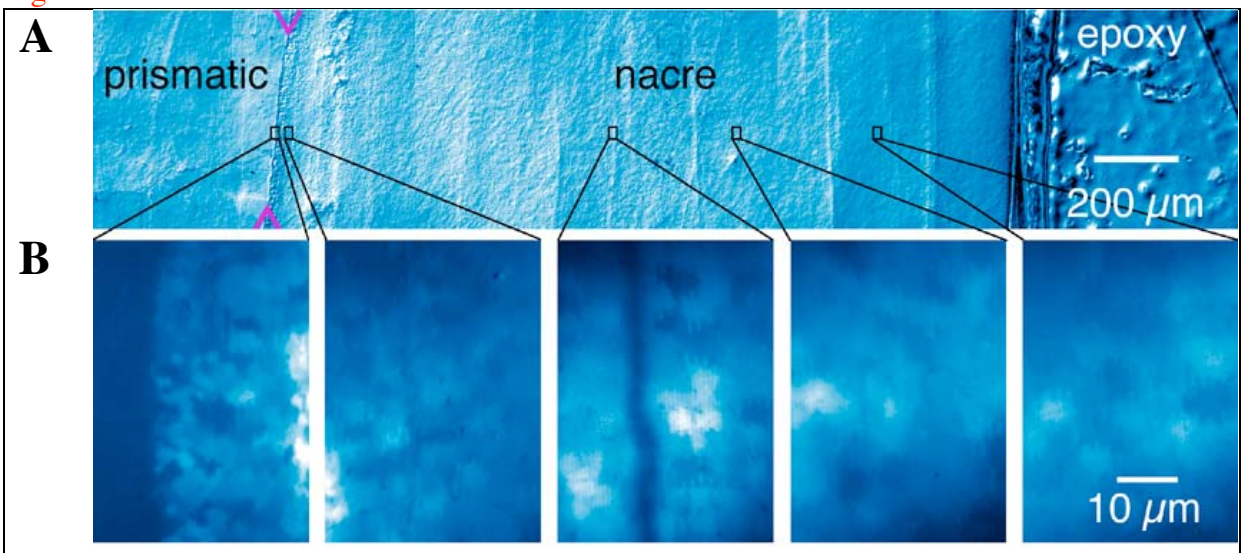

Figure 10. (**A**) Visible light microscopy composite micrographs of a polished section of red abalone shell, acquired in differential interference contrast mode. The nacre growth direction was 30° from the sample surface normal. The line between two magenta arrowheads is the prismatic-nacre boundary. The black rectangles outline the areas in which the O maps in (B) were acquired with SPHINX. (**B**) Series of oxygen PIC maps, obtained by digital ratio of images acquired at 534 and 530 eV, π* and pre-edge, respectively. PIC is clearly detectable across the entire thickness of the nacre layer. The central PIC map was acquired across one of the vertical lines evident in the optical image, which do not appear to affect tablet order or contrast. To enhance contrast in bulk nacre all raw grayscale maps were leveled and converted to a blue quadtone.

Figure 11

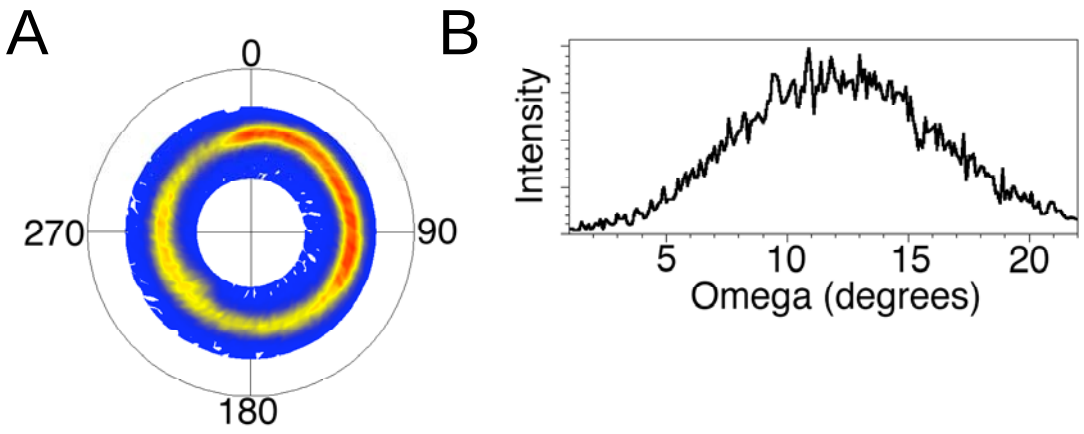

Figure 11. (**A**) X-ray diffraction pole figure indicates random orientation of nacre tablets in the ab-plane. (**B**) Rocking curve taken on the (002) Bragg peak on a piece of red abalone nacre. The 22º footprint of the rocking curve indicates that the c-axis variation in bulk nacre varies by ±11º, with instrument resolution better than 0.1º.